



Article

Detecting Offshore Drilling Rigs with Multitemporal NDWI: A Case Study in the Caspian Sea

Hui Zhu ^{1,2,3}, Gongxu Jia ^{1,2,3}, Qingling Zhang ^{4,*}, Shan Zhang ^{1,2,3}, Xiaoli Lin ^{1,2,3} and Yanmin Shuai ^{2,5,6}

¹ State Key Laboratory of Desert and Oasis, Xinjiang Institute of Ecology and Geography, Chinese Academy of Sciences, Urumqi 830011, China; zhuhui17@mailsucas.ac.cn (H.Z.); jiagongxu19@mailsucas.ac.cn (G.J.); zhangshan18@mailsucas.ac.cn (S.Z.); Linxiaoli18@mailsucas.ac.cn (X.L.)

² Xinjiang Institute of Ecology and Geography, Chinese Academy of Sciences, Urumqi 830011, China; shuaiym@ms.xjb.ac.cn

³ University of Chinese Academy of Sciences, Beijing 100039, China

⁴ School of Aeronautics and Astronautics, Sun Yat-sen University, Shenzhen 518107, China

⁵ Research Center for Ecology and Environment of Central Asia, Urumqi 830011, China

⁶ College of Surveying and Mapping and Geographic Science, Liaoning Technical University, Fuxin 123000, China

* Correspondence: zhangqingling@mail.sysu.edu.cn; Tel.: +86-181-2709-5863

Abstract: Offshore drilling rigs are the foundation of oil and gas exploitation in water areas. Their spatial and temporal distribution, state attributes and other information directly reflect the exploitation level of regional oil and gas resources. Therefore, it is very important to build an automatic detecting method for offshore drilling rigs with good performance to accurately capture the temporal and spatial distribution and state of oil and gas exploitation activities. At present, there are two main groups of methods for offshore drilling rigs: invariant feature-based methods and nighttime firelight-based methods. Methods based on invariant location are more subjective in terms of their parameter settings and require intensive computation. Nighttime light-based methods are largely unable to identify offshore drilling rigs without associated waste gas ignition. Furthermore, multiple offshore drilling rigs in close proximity to one another cannot be effectively distinguished with low spatial resolution imagery. To address these shortcomings, we propose a new method for the automatic identification of offshore drilling rigs based on Landsat-7 ETM+ images from 2018 to 2019, taking the Caspian Sea as the research area. We build a nominal annual cloud and cloud shadow-free Normalized Difference Water Index (NDWI) composite by designing an optimal NDWI compositing method based of the influence of cloud and cloud shadow on the NDWI values of water, bare land (island) and offshore drilling rigs. The classification of these objects is simultaneously done during the compositing process, with the following rules: water body ($\text{Max_NDWI} > 0.55$), bare land (island) ($\text{Min_NDWI} < -0.05$) and offshore drilling rig ($0 < \text{Mean_NDWI} < 0.4$). A threshold segmentation and postprocessing were carried out to further refine the results. Using this method, 497 offshore platforms were automatically identified using a nominal annual cloud and cloud shadow-free NDWI composite image and Google Earth Engine. Validation using Sentinel-2 Multispectral Imager (MSI) and Google Earth images demonstrated that the correct rate of offshore drilling rig detection in the Caspian Sea is 90.2%, the missing judgment rate is 5.3% and the wrong judgment rate is 4.5%, proving the performance of the proposed method. This method can be used to identify offshore drilling rigs within a large water surface area relatively quickly, which is of great significance for exploring the exploitation status of offshore oil and gas resources. It can also be extended to finer spatial resolution optical remote sensing images; thus small-size drilling rigs can be effectively detected.

Keywords: energy production; natural resource; optical remote sensing; time series analysis; oil market; NDWI; Caspian Sea; Landsat-7 ETM+



Citation: Zhu, H.; Jia, G.; Zhang, Q.; Zhang, S.; Lin, X.; Shuai, Y. Detecting Offshore Drilling Rigs with Multitemporal NDWI: A Case Study in the Caspian Sea. *Remote Sens.* **2021**, *13*, 1576. <https://doi.org/10.3390/rs13081576>

Academic Editor: Lalit Kumar

Received: 22 February 2021

Accepted: 2 April 2021

Published: 19 April 2021

Publisher's Note: MDPI stays neutral with regard to jurisdictional claims in published maps and institutional affiliations.



Copyright: © 2021 by the authors. Licensee MDPI, Basel, Switzerland. This article is an open access article distributed under the terms and conditions of the Creative Commons Attribution (CC BY) license (<https://creativecommons.org/licenses/by/4.0/>).

1. Introduction

Petroleum is often regarded as the blood of modern industry. With the development of industry, world demand for energy, including oil and gas, has been constantly increasing. As onshore oil and gas exploration becomes increasingly mature, the growth of global oil and gas reserves slows down. The scale of newly-discovered oil and gas resources becomes smaller and their exploitation more difficult [1]. Consequently, more and more attention has been paid to exploring and exploiting offshore oil and gas resources in recent years. According to the statistical data of the U.S. Energy Information Administration (EIA), offshore production accounted for nearly 30% of global crude oil output in 2015. Therefore, investigating and monitoring oil and gas exploitation activities in the sea is of great significance to understanding the development of oil and gas resource extraction and understanding global energy development.

Traditional reports of oil and gas resource data are mainly included in national-scale statistics [2], such as BP World Energy Statistics [3], International Energy Statistics of the U.S. EIA [4], World Bank database [5], etc. Such statistical reports often poorly reflect the temporal and spatial distribution of oil and gas exploitation activities due to human factors. In contrast, remote sensing has the characteristics of a short revisiting period, timeliness and large area synchronous observation, which makes it possible to monitor the development of offshore drilling rigs with temporal and spatial details. Furthermore, the powerful spatial data management and spatial analysis functions of modern Geographic Information Systems (GIS) provide powerful technical support to manage related spatial data. At the same time, with the development of cloud platform technology, e.g., remote sensing cloud computing platforms such as the Google Earth Engine (GEE), have recently emerged, creating the possibility of rapid and accurate extraction of geographic information on a large scale from big remote sensing data [6]. Therefore, remote sensing technologies and GIS are being more and more widely used to extract data about offshore drilling rigs.

Existing algorithms for identifying and monitoring offshore drilling rigs with remote sensing mainly focus on the following two aspects: (1) eliminating false alarms to determine offshore drilling rigs according to their position and shape invariant characteristics in multitemporal remote sensing images; and (2) high temperature and brightness of the associated waste gas flames at night (Figure 1). However, there are other advanced techniques such as Machine Learning algorithms. With the wide application of Convolutional Neural Networks (CNNs) in ship target detection on the sea [7–10], this technology has been applied to oil and gas platform recognition [11].

A few studies have been carried out to identify offshore drilling rigs based on their location invariant feature in Synthetic Aperture Radar (SAR) data. These researchers developed a two-parameter false alarm algorithm to identify the location of potential offshore drilling rigs with SAR images first, and then eliminate the false alarm with multiphase SAR data to improve the predictions of offshore drilling rigs in the South China Sea [12–14]. Cheng et al. [15] proposed a method based on the triangular invariant rule to identify offshore drilling rigs with SAR and reported improved detection accuracy of offshore drilling rigs in the South China Sea. Wan et al. [16] compared the shape differences between ships and offshore drilling rigs in SAR data to improve detection accuracy. Wong et al. [17] developed a cloud-native geoprocessing algorithm to automatically detect and extract offshore oil platforms in the Gulf of Mexico using synthetic aperture radar and the Google Earth Engine. Zhang et al. [18] proposed an automatic extraction method for offshore platforms in single SAR images based on a dual-step-modified model.

Passing ships are the main source of false alarm in offshore drilling rig identification. Meng and Xing [19] attempted to map offshore drilling rigs and ships using Landsat remote sensing images taken within a single time phase, but the results showed that single time phase optical images could not distinguish the two well. Cheng et al. [20] utilized the high brightness of lighting facilities and associated high temperature of waste gas combustion flames in oil and gas exploitation activities at night to map the target area of offshore drilling rigs in the South China Sea based on the Defense Meteorological Satellite Pro-

gram/Operational Linescan System (DMSP/OLS) nighttime light images. They performed multilayer screening based on multitemporal Landsat-8 OLI (band 6) images to determine the presence of offshore drilling rigs. Liu et al. [21] adopted a multilayer screening optimization and multitemporal overlapping comparison strategy to automatically identify offshore drilling rigs in the Persian Gulf, the Gulf of Mexico and the Gulf of Thailand, with full consideration to the characteristics of spectra, texture, shape and location of offshore drilling rigs in Landsat-8 OLI (band 6). Zhao et al. [22] identified offshore drilling rigs in the South China Sea by using a multislicing window threshold and multitemporal images superposition comparison based on Landsat images. Li et al. [23] proposed a critical value algorithm for convolution operation based on phase 2 NPOESS Preparatory Project/Visible Infrared Imaging Radiometer Suite (NPP/VIIRS) imaging products. They identified offshore drilling rigs in the Northern part of the South China Sea. Sun et al. [24] conducted a long time series analysis of offshore drilling rigs in the South China Sea based on multitemporal and multisource remote sensing image data, including Landsat and SAR data. An exploratory analysis of the relationship between the total nighttime light of offshore drilling rigs and oil and gas production was established based on DMSP/OLS nighttime light images. Fan et al. [25] proposed a new automatic extraction algorithm for offshore platforms in the Bohai area based on multispectral image of the Gaofen-2 (GF-2) MSS sensor. As is known to all, existing detection methods of offshore platforms based on optical remote sensing images often rely on a large number of time series images. In order to improve the accuracy of platform detection with single images, Zhu et al. [26] proposed a platform detection method based on a Harris detector and intensity texture feature image from a Sentinel-2 L2A Image.

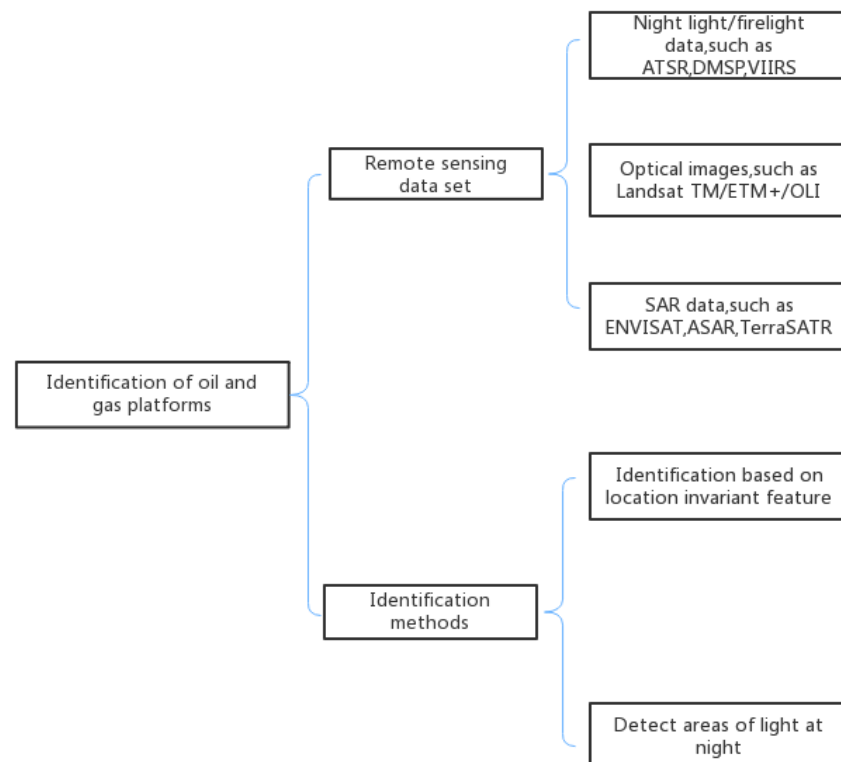


Figure 1. Research framework of offshore drilling rig identification.

Waste gases during oil and gas extraction processes are often hard to collect, and burning them is a routine way to prevent environment damage. In 1978, the associated waste gas flame was first observed on DMSP/OLS night-time light image data [27]. Thereafter, Stroppiana et al. [28] applied a context automatic recognition algorithm to generate the first global-scale spatiotemporal distribution map of fire points based on thermo-infrared Advanced Very High Resolution Radiometer (AVHRR) image data. Chowdhury et al. [29]

attempted to test the possibility of detecting the associated waste gas combustion sources in Alberta using Sequential Maximum Angle Convex Cone (SMACC) with the short-wave infrared of 1.6 μm and 2.2 μm Landsat-8 images. The results show that the recognition effect of daytime Landsat-8 images for detecting the associated waste gas flames is not good. Casadio et al. [30] extracted offshore drilling rigs in the North Sea area in 2008 by using the short-wave infrared band (1.6 μm) at nighttime Along Track Scanning Radiometer (ATSR), and the extraction results were highly correlated to the reported oil and gas production in the North Sea region. Anejionu et al. [31] studied the spatial and temporal distribution of oil-associated waste gas combustion sources in the Niger Delta from 2000 to 2014 with a double threshold segmentation algorithm applied to the mid-infrared bands (3.96 μm) of nighttime Moderate-resolution Imaging Spectroradiometer (MODIS). Elvidge et al. [32] used the characteristics of associated waste gas flames on DMSP/OLS false color composite images, and visually interpreted the spatial distribution of relatively stable waste gas ignition points in the world at the country scale from 1992 to 2008. Elvidge et al. [33] proposed a network function virtualization (VNF) algorithm based on the short and medium infrared bands of National Polar-orbiting Operational Environmental Satellite System Preparatory Project/Visible infrared Imaging Radiometer (NPP/VIIRS) images and the Planck fitting formula to automatically extract global thermal anomalies. Elvidge et al. [34] refined the thermal anomalies extraction VNF algorithm, extracted global waste gas combustion sources and classified them into upper, downstream and liquefied natural gas (LNG) site ignition points with high-resolution NPP/VIIRS images.

However, there are some major drawbacks with the approaches mentioned above. For the algorithms based on SAR images and Landsat images, the parameters were set subjectively and required intensive computation. At the same time, multiphase data comparison also poses a new challenge to the quality and quantity of remote sensing data. Offshore drilling rig identification based on associated waste gas flames mainly uses the near-infrared and short-wave infrared bands of NPP/VIIRS, MODIS and AVHRR images, causing those without gas combustion to be largely unidentifiable. Moreover, because the spatial resolutions of the mentioned remote sensing images are generally low, it is especially difficult for multiple offshore drilling rigs gathered closely together to be accurately differentiated.

We propose a new method for offshore drilling rig extraction in the Caspian Sea, aiming to overcome these drawbacks. We build our method based on an observed phenomenon: a drilling rig set up above the sea surface will cause a significant drop of the Normalized Difference Water Index (NDWI) calculated with satellite observations in that specific water area. We first examine the maximum, minimum and average NDWI values of seawater, offshore drilling rigs and bare land (islands) in the Landsat-7 ETM+ images based on samples collected for these three groups, and then build nominal annual cloud and cloud shadow-free image composites, based on the analysis of the influence of cloud and cloud shadow on the NDWI values of water, bare land (island) and offshore drilling rigs. Based on these cloud and cloud shadow-free NDWI composites, we design a set of classification rules to distinguish offshore drilling rigs from the other two groups.

To test this method, we extract the offshore drilling rigs in 2018 in the Caspian Sea based on our method and verify the extraction accuracy. The results show that this method has good performance.

2. Study Area

2.1. Physical Geographical Background

The Caspian Sea, the largest saltwater lake in the world, is located between 44.69°~54.07° E and 36.58°~47.11° N. It sits at the junction of Europe and Asia, bordering Kazakhstan, Turkmenistan, Iran, Azerbaijan and Russia (Figure 2). The length of the lake is about 1200 km from north to south, with an average width of 320 km from east to west. The shoreline of the lake is about 7000 km in length, covering 371,000 square kilometers. The

Caspian Sea has an ecosystem similar to that of the ocean, with a thriving shipping industry, and is a “sea trail lake” geographically [35].

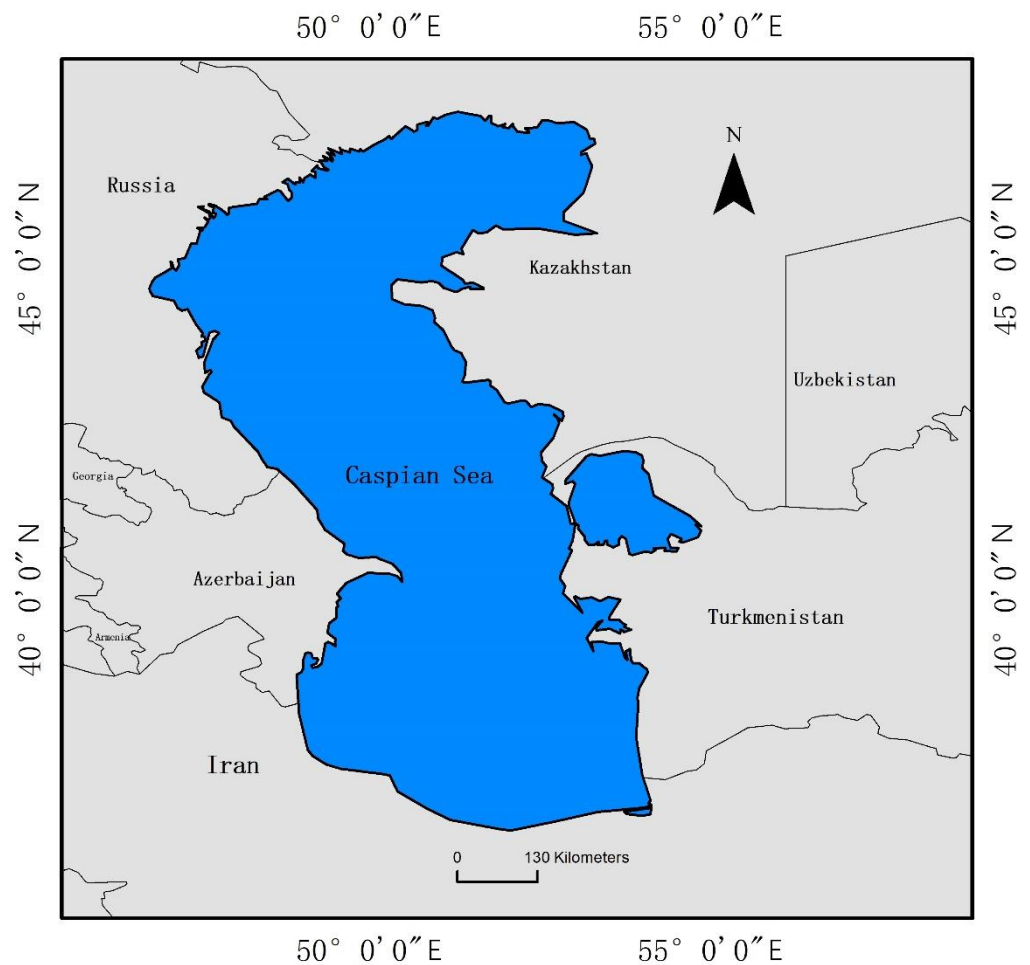


Figure 2. The location of Caspian Sea.

2.2. Oil and Gas Resource Endowment

The Caspian Sea region consists of four major geological basins: the northern, central and southern Caspian basins, and the Ustel basin in the north. Territorial disputes and limited exploration techniques in offshore areas make it difficult to determine the Caspian Sea oil and gas reserves. Based on field data, onshore and offshore fields in the broad Caspian Basin are thought to hold 48 billion barrels of oil and 292 trillion cubic feet of waste gas, respectively (U.S. EIA, year) (Table 1). Since the reserves figure includes both proven and probable reserves, it tends to be overestimated. Most of these reserves are offshore or near the Caspian Sea coasts, especially near the north coast. The EIA estimates that 41% of the total Caspian oil and associated gas condensates (19.6 billion barrels) and 36% of the waste gas (106 trillion cubic feet) are offshore, with most of the offshore oil in the northern Caspian and most of the offshore gas in the southern Caspian. Another 35% of oil (16.6 billion barrels) and 45% of waste gas (130 trillion cubic feet) can be found onshore within 100 miles of the coasts, particularly in Russia’s North Caucasus. The remaining 12 billion barrels of oil and 56 trillion cubic feet of waste gas are scattered farther onshore in the large Caspian Basin, mainly in Azerbaijan, Kazakhstan and Turkmenistan.

Table 1. Caspian basins proved and probable reserves

Country	Crude Oil and Lease Condensate (Billion Barrels)	Natural Gas (Billion Cubic Feet)
Azerbaijan	8.5	51
The Caspian offshore parts	6.8	46
The Land parts	1.7	5
Iran	0.5	2
The Caspian offshore parts	0.5	1
The Land parts	(s)	1
Kazakhstan	31.2	104
The Caspian offshore parts	15.7	36
The Land parts	15.5	68
Russia	6.1	109
The Caspian offshore parts	1.6	14
The Land parts	4.5	95
Turkmenistan	1.9	19
The Caspian offshore parts	1.1	9
The Land parts	0.8	10
Uzbekistan	(s)	7
The Caspian offshore parts	0	0
The Land parts	(s)	7
The Caspian basin	48.2	292
The Caspian offshore parts	19.6	106
The Land parts	28.6	186

Note: (s) indicates that the number is extremely small relative to the statistical value. The Caspian offshore parts refer to the oil and gas fields in the waters of the Caspian Sea. The Land parts refer to the oil and gas fields in Caspian Basin but not in the waters. **Data source:** the U.S. Energy Information Administration (EIA) [36].

The Caspian Sea region is one of the oldest oil-producing regions in the world and an increasingly important source of global energy production. The region is rich in oil and gas resources, both from offshore deposits in the Caspian Sea and onshore oil fields in the Caspian Basin. The legal status of the Caspian Sea region is complicated by the lack of consensus on whether it should be defined as a “sea” or a “lake”. In each case, different international laws would apply. As a result, changing legal and regulatory frameworks create uncertainty for foreign companies to invest in natural resources. For example, the lack of an agreed maritime boundary between Turkmenistan, Azerbaijan and Iran hampers geological exploration in the southern Caspian Basin. The existing data related to oil and gas resources in the Caspian Sea that can be shared are mainly based on national statistical data. A timely, accurate and comprehensive grasp of the status quo, history and trends of the exploitation of oil and gas resources in the region is of great significance to the regional security of central Asia. Therefore, we chose the Caspian Sea as the study area.

3. Methodology

The offshore drilling rigs in the Caspian Sea are usually small in size (generally 120 m × 70 m), and most of them have no associated gas vent burning torch equipment, such as the Shah Deniz Oil Field and the Azeri-Chirag-Guneshli (ACG) Oil field. At present, there are some studies on the automatic identification of offshore drilling rigs based on remote sensing images. Centering on the features of offshore drilling rigs with unchanged spatial position, shape and size, multistage and multisource remote sensing data is adopted to extract offshore drilling rigs [20,21,23,37]. These kinds of methods show good detection performance for offshore drilling rigs on the whole, but relatively poor performance for small platforms without associated waste gas burning flames. The current study proposes a new algorithm based on NDWI composed with multitemporal Landsat-7 ETM+ images to automatically detect offshore drilling rigs.

3.1. Data Sources and Data Preprocessing

The remote sensing data sources used in this study mainly include Landsat-7 ETM+ data, Sentinel-2 Multispectral Imager (MSI) data, Google Earth image, and global ignition point dataset generated with the VIIRS data. Except for the ignition point data from the data set published in the existing research [34], the other data are from GEE database data (Table 2). According to the location of study area, we chose 596 Landsat-7 ETM+ images taken from January 2018 to December 2019 and 98 Sentinel-2 MSI images taken from 2016 to 2019. The Landsat series of sensors are widely used for long-time continuous observation with high geometric accuracy (less than 30 m), even in areas with large topographic relief [38]. The Landsat-7 ETM+, one of the Landsat series, has the longest observation time (1999–Present). Although 22% of the pixels were missing because of the Scan Line Corrector (SLC) failure in 2003, the ETM+ data is also widely used in land-cover change analyses [37,39,40]. Zhang et al. [41] and Morel et al. [39] proposed an effective method to fill in the missing data. Landsat-7 ETM+ data is the main remote sensing data source used in the offshore drilling rig identification and monitoring algorithm proposed in this study. It was noted that some areas of our study area were not covered by Landsat-7 ETM+ images, and these areas were not considered for testing the proposed method. Sentinel-2 MSI data and Google Earth image data are mainly used to verify the accuracy of identifying offshore drilling rigs, considering their relatively finer spatial resolutions. In the analysis of dynamic monitoring results of offshore drilling rigs in the Caspian Sea, a Google Earth image was used for partial verification of the near shore area, and Sentinel-2 MSI images were used for visual interpretation and verification. The 2018 VIIRS ignition point data was used to identify the Caspian offshore drilling rigs and evaluate the results of the present study. The data used in this study and the Landsat-7 ETM+ images coverage of the Caspian Sea for our method are shown in Table 2 and Figure 3.

Table 2. Remote Sensing data used in this study.

Data Set	Data Name	Spatial Resolution	Data Source
Landsat data	Landsat-7/ETM+	30 m	GEE [42]
Night-light data	VIIRS/DNB	About 500 m	NOAA [43]
High-resolution data	Sentinel-2 MSI	10 m	GEE [44]
	DigitalGlobe imagery	/	Google Earth

Note: Google Earth Engine (USGS), National Oceanic and Atmospheric Administration (NOAA).

Considering the relatively large scale of the Caspian Sea region, most of our remote sensing data processing and analysis are carried out on the Google Earth Engine (GEE) cloud computing platform. GEE provides not only a mass remote sensing data archive, but also big data computing facilities, enabling large-scale remote sensing studies. The Landsat-7 ETM+ data are provided by the Earth Resources Observation and Science (EROS) Center and are archived on the GEE Cloud platform. We use only Landsat 7 Collection 1 Tier 1 and Real-Time data to reduce the impact of registration errors, critical for time series synthesis. Six bands of Landsat ETM+ were used in this study: blue (band 1: 0.45–0.52 μm), green (band 2: 0.53–0.61 μm), red (band 3: 0.63–0.69 μm), near-infrared (band 4: 0.78–0.90 μm) and two mid-infrared (band 5 and 7: 1.55–1.75 μm and 2.09–2.35 μm). Each Landsat-7 ETM+ L1T scene is approximately 185 km \times 85 km, and since May 2003, 22% pixels have been lost in the repeated stripe pattern along with the scan due to ETM+ Scan Line Corrector (SLC) failure [45].

In ETM+ images, low-quality pixels often lack full spectral bands, especially at the image edges. Before generating the NDWI composite, these pixels must be first identified and removed. We generate a low-quality ETM+ pixel mask (including gaps caused by SLC-OFF) by examining bands 1–5 and 7: If the product is equal to 0, the pixel is of low quality and is discarded [41]. Additionally, clouds and shadows seriously contaminate

Landsat images in the late stage [46]. We adopt the FMASK algorithm to remove clouds and shadows from Landsat images to reduce their influence on the NDWI index [47].

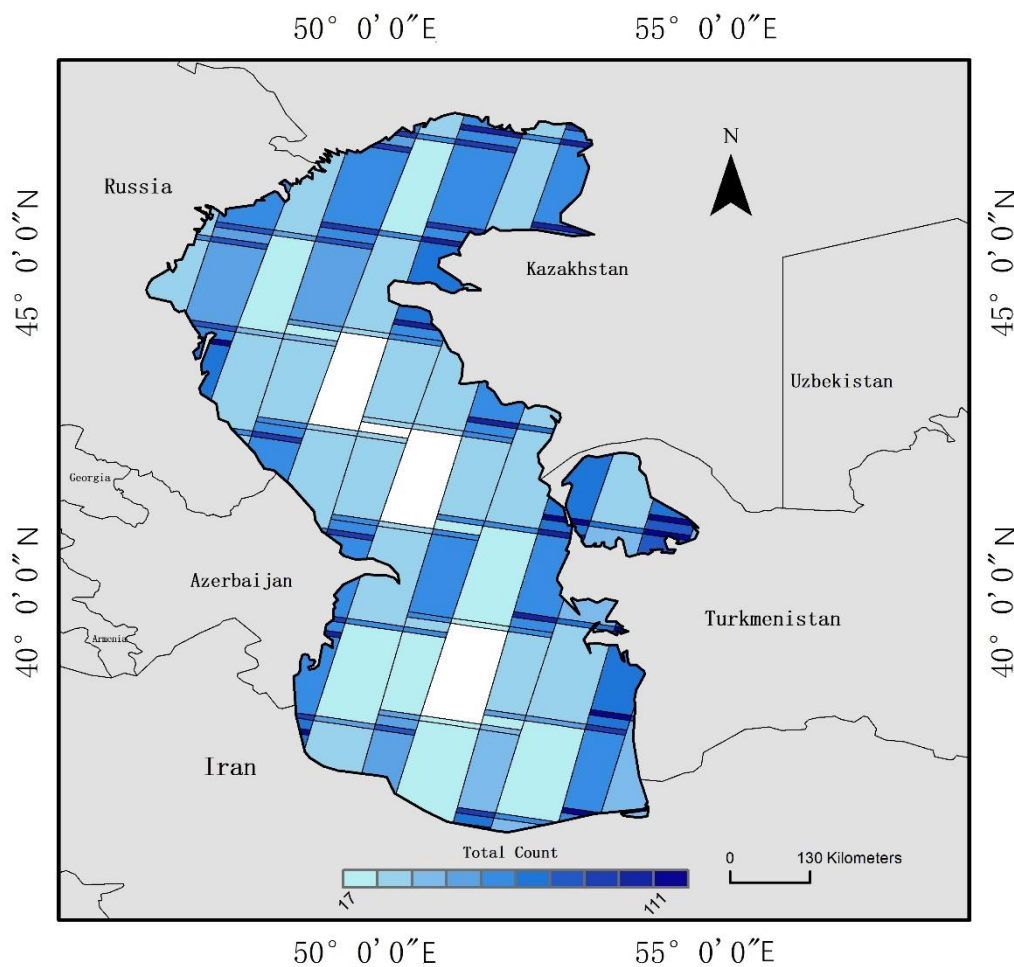


Figure 3. The total count of Landsat ETM+ images coverage of Caspian Sea in 2018 and 2019. Note: there are no data in the white areas.

3.2. Offshore Drilling Rig Appearance in Remote Sensing Images

An offshore drilling rig is the infrastructure for drilling, extracting, processing and temporarily storing crude oil and natural gas. It is the carrier of offshore oil and gas production activities [25]. The metal concrete structure and associated waste gas incineration characteristics of the offshore drilling rigs make them show high reflectivity, in contrast to the seawater background in remote sensing images [25]. However, due to the small size of offshore drilling rigs, weak image features and the vast ocean background with noise (cloud, cloud shadow, etc.) and false alarms (passing vessels), the accurate detection of spatial information of offshore oil and gas production platforms from images still faces great challenges [21].

Offshore drilling rigs are mostly metal structures, and their NDWI value is much smaller than that of water, which is reflected in the obvious difference in brightness between offshore drilling rigs and the water background in remote sensing images (Figure 4d–f). Figure 4d–f shows the minimum, mean and maximum NDWIs, calculated from a series of images taken within one year, offshore drilling rigs and the background water, respectively. In the maximum NDWI composite image (Figure 4f), the difference between the offshore drilling rigs and the background (water) is most obvious. Thus, the maximum value NDWI composites can be used to extract offshore drilling rigs.

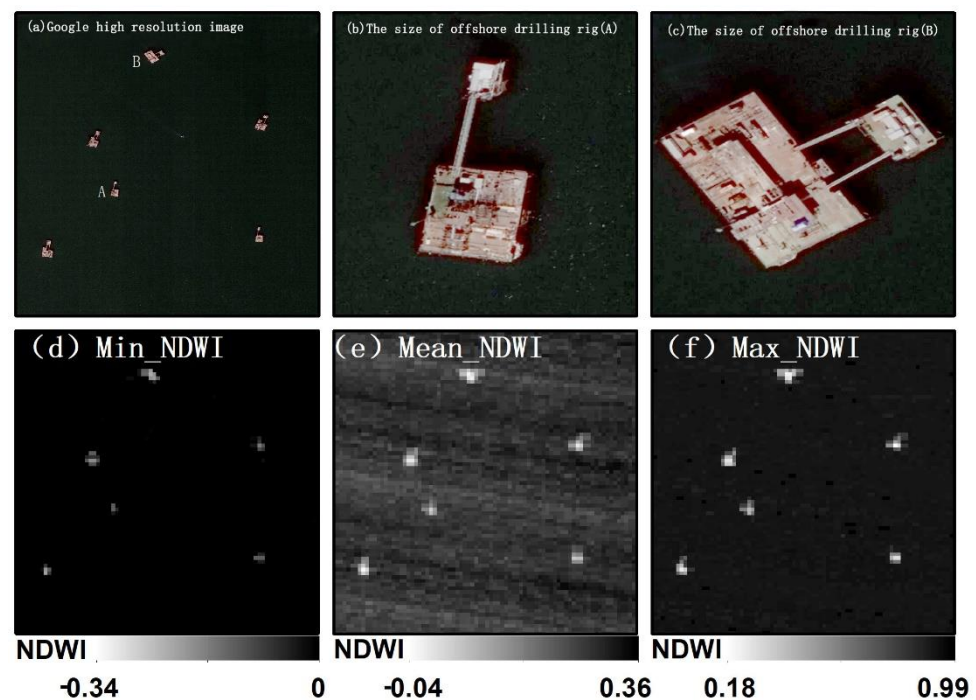


Figure 4. Caspian offshore drilling rig: (a) is offshore drilling rigs of the ACG oil and gas fields in Google high-resolution image; (b,c) are sizes of offshore drilling rigs; (d,e,f) are offshore drilling rigs in different NDWI synthesis methods.

3.3. Establishment of NDWI Classification Rule

3.3.1. Distinguishability Analysis of Different Water Indexes on Drilling Platform, Water and Bare Land

In this section, we analyze the distinguishability of NDWI, NDWI-NDVI (Normalized Difference Vegetation Index) [48] and Modified NDWI (MNDWI) [49] to drilling platform, water and bare land. Using Sentinel-2 L1C image on GEE platform, we randomly select 60 sample areas of offshore drilling rigs, water and bare land. Then, we calculate the mean value of three water body indexes for each small area and obtain the water index changes of three features (drilling rig, water and bare land) (Figure 5).

For offshore drilling rigs, we can see that the changes of NDWI and MNDWI are more consistent; the NDWI value is slightly lower than MNDWI, but the ndwi-ndvi value is lower. For the water body, the values of NDWI-NDVI, NDWI and MNDWI increase in turn. For the bare land, the values of NDWI-MDVI, NDWI and MNDWI decrease in turn. It can be seen that for the drilling rigs and water body, the minimum values of the three water body indexes on the drilling platform are greater than the maximum values on the water body; for the drilling rigs and bare land, the NDWI and MNDWI values of most drilling platforms are larger than those of bare land, but the difference of NDWI-NDVI values between these drilling platforms and bare land is not obvious. In conclusion, NDWI-NDVI has the lowest discrimination, and NDWI and MNDWI have similar discrimination. Therefore, we choose NDWI as the water index for our method.

3.3.2. NDWI

NDWI is the normalized difference between the green band (band 2) and near-infrared band (band 4) [50], which can enhance water in remote sensing images. NDWI is widely used in water recognition. Its formula is:

$$\text{NDWI} = \frac{\rho_{\text{Green}} - \rho_{\text{NIR}}}{\rho_{\text{Green}} + \rho_{\text{NIR}}} \quad (1)$$

where ρ_{NIR} represents the reflectivity of the near-infrared band and ρ_{Green} represents the reflectivity of the green band. Water bodies often show high NDWI values. As a comparison, the NDWI values of offshore drilling rigs are much lower, and there is a large difference between them (Figure 4d–f).

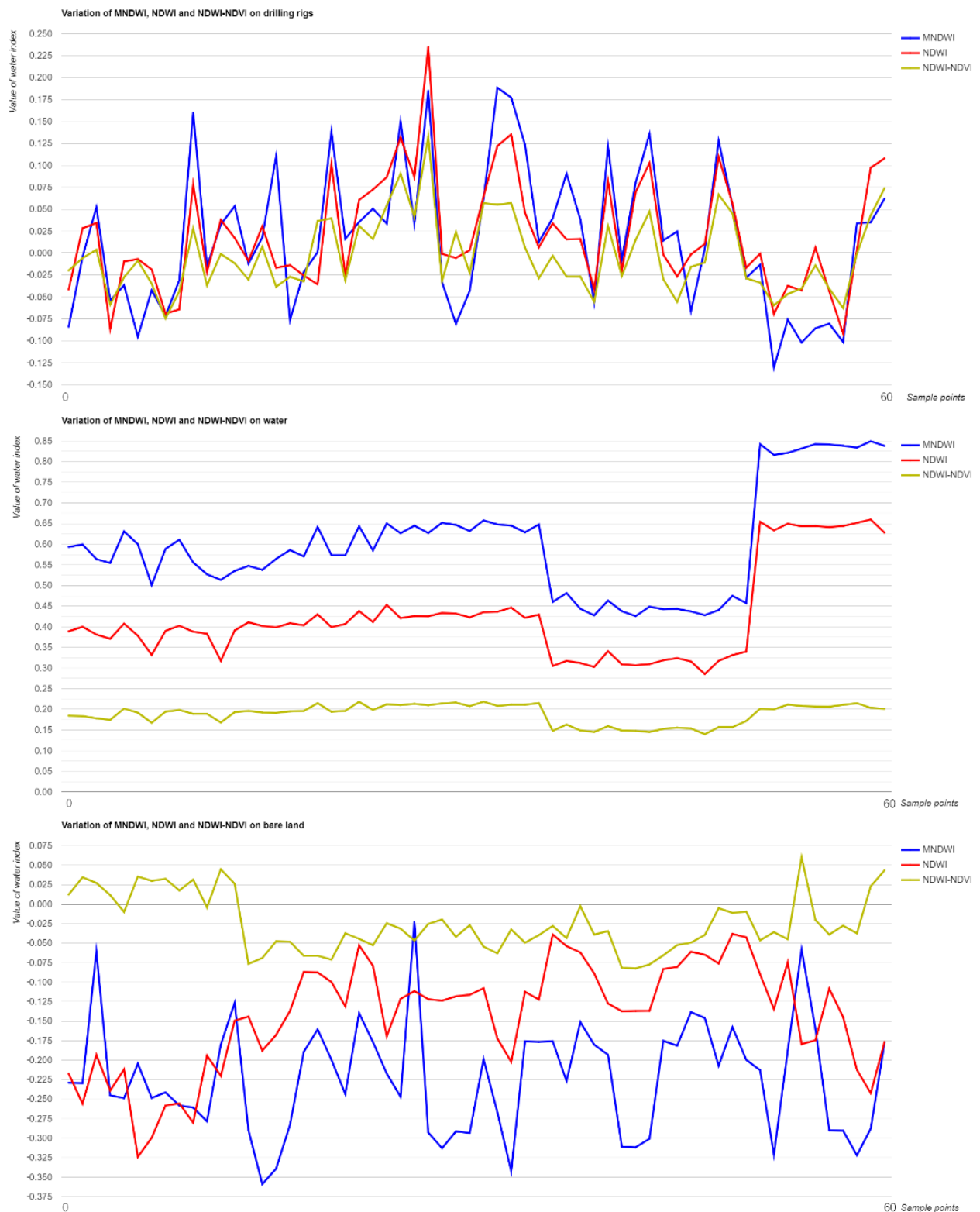


Figure 5. Changes of NDWI, MNDWI and NDWI-NDVI on drilling platform, water body and bare land.

Since 1999, multispectral Landsat-7 ETM+ data with a spatial resolution of 30 m have been archived. However, cloud and cloud shadow pollution, as well as the lack of algorithms to analyze them, greatly hindered their use [41]. At the same time, clear images are often rare, especially in tropical areas with persistent thick cloud cover [51]. Therefore, good image pixels with useful information in some polluted images are often not well utilized.

Many algorithms have been developed to automatically detect and remove clouds and associated shadows in Landsat images [52,53]. These advanced algorithms detect clouds and cloud shadows with higher and higher accuracy, but none can achieve a 100% screening effect. Consequently, residual clouds and cloud shadows, especially thin clouds and associated shadows, can still remain. To make better use of high-quality pixels in images that may be partly polluted by clouds and cloud shadows, we propose a multitemporal image compositing algorithm. Pixel-scale satellite image compositing was initially developed for Advanced Very High-Resolution Radiometer (AVHRR) time series by automatically picking up image pixels free of cloud or cloud shadow pollution. This technology aims to generate a high-quality composite image by picking up clear pixels from other periods, even if there is no single clear image in a specific period. All the pixels that are not completely polluted can be better utilized. The largest normalized difference vegetation index (NDVI) and the maximum apparent temperature method [54] are commonly used. In 2015, Zhang et al. [41] modified the maximum NDVI value compositing method to consider to the underlying earth surface (vegetated land, bare land and water) and applied different compositing criteria individually to generate a final NDVI composite image. In this study, we modify the algorithm of Landsat's nominal annual NDVI composite proposed by Zhang et al. to generate the optimal cloud-free NDWI images based on Google Earth Engine (GEE) using Landsat-7 ETM+ data.

3.3.3. Effects of Clouds and Cloud Shadows on NDWI

To remove the influence of clouds and cloud shadows on NDWI, we first examine their disturbance to NDWI values. The effect of cloud and cloud shadow on NDWI values depends largely on the underlying surface (Figure 6). There are three major types of objects in the region of the Caspian Sea: water, bare land (mainly islands) and offshore drilling rigs. Among them, bare land mainly refers to the islands inside the Caspian Seawater and seasonally exposed lands along the Caspian Sea coasts. Over the water surface, clouds will reduce the NDWI value, while cloud shadow has relatively little influence on its NDWI value (Figure 6a). Over the bare land surface, the NDWI value will increase to different degrees due to the influence of cloud and cloud shadow (Figure 6b), and cloud thickness has different degrees of influence on the NDWI value. Compared with water and bare land, the spatial distribution of offshore drilling rigs is discontinuous. To compare the influence of cloud and cloud shadow on offshore drilling rigs, we select images with cloud (shadow) and without cloud (shadow) in the same area in order to conduct a statistical analysis on the NDWI values of different offshore drilling rigs (Figure 6). In Figure 6c, the blue line represents the NDWI value of the offshore drilling rigs under cloudless conditions and the orange line represents the NDWI value of the offshore drilling rigs under cloudy (shadowy) conditions. It can be seen that due to the influence of cloud and shadow, the NDWI value of offshore drilling rigs will decrease to a certain extent. Compared with the NDWI curve of water and bare land, the NDWI curve of offshore drilling rigs fluctuates greatly, mainly due to the mixed noise of water around the offshore drilling rigs.

The NDWI values of a water body, bare land and offshore drilling rig pixels under different clouds and cloud shadows were calculated. The results showed that the maximum NDWI value should be used to select clear water pixels in a time series, but for bare land, the criteria of minimum NDWI value should be adopted. For offshore drilling rigs, the NDWI value is between water and bare land, and due to strip and other problems of Landsat 7 ETM+ images, the criterion of mean NDWI value is adopted (Table 3). Based on these observations, we develop the optimal NDWI criteria rather than the single maximum

NDWI criteria to describe the NDWI of different ground objects of water in the clear sky (Table 3).

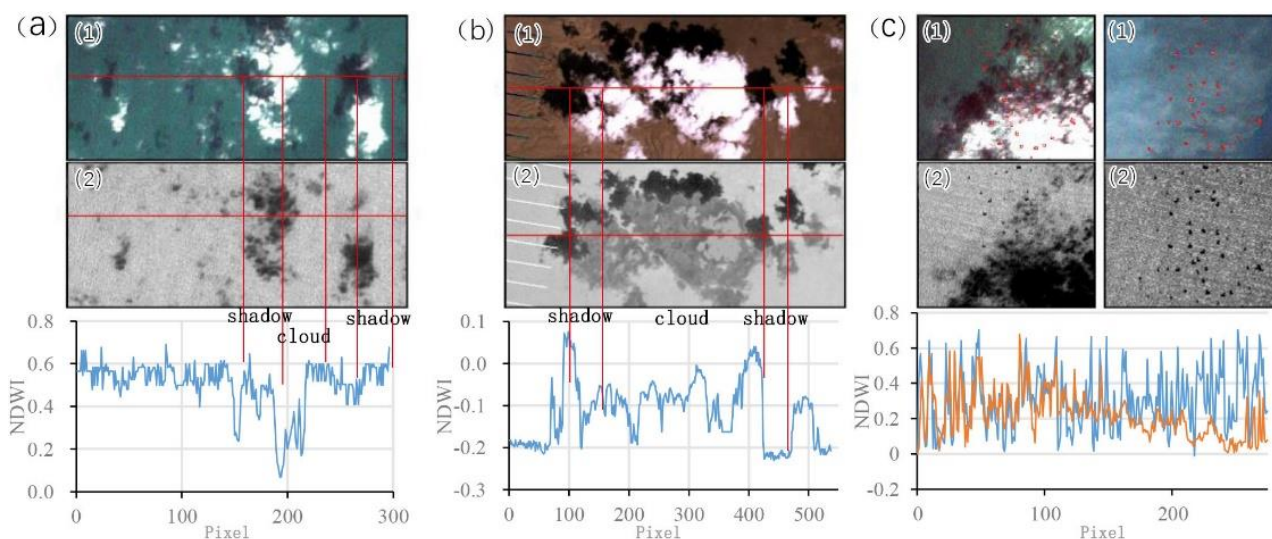


Figure 6. Clouds and cloud shadows and their effects on NDWI. (a): over the water surface, (b): over bare land surface, (c): over offshore drilling rigs. (1) True color Landsat 7 ETM+ image. (2) Landsat 7 ETM + NDWI image. The images (c) on the left and right sides are images of the offshore drilling rigs with and without clouds (shaded).

Table 3. The impacts on NDWI from clouds and cloud shadows over different landcover types.

Ground object	NDWI	Cloud Effect	Shadow Effect	Optimal NDWI
Water	High	↘	↘	Maximum NDWI
Bare land	Low (negative)	↗	↗	Minimum NDWI
Offshore drilling rigs	Between water and bare land	↘	↘	Mean NDWI

3.3.4. NDWI Feature Extraction for the Classification of Different Objects

Offshore drilling rigs are fixed in location and can be operated for a long time once built (generally around 20 years). Although there are often many ships in the Caspian Sea, their positions are generally not fixed over a period of time. The optimal NDWI compositing method proposed in this paper based on Landsat images for two consecutive years can also effectively avoid false alarms caused by ships. In the analysis of the influence of cloud and cloud shadow on the water, bare land and offshore drilling rigs in Section 3.3.3, it can be seen that the influence of clouds and cloud shadows on the three types of objects is different. To eliminate or minimize the impact of clouds and cloud shadows on NDWI to compose the optimal NDWI images, different ground object types in the Caspian Sea surface should first be distinguished. Then, the optimal NDWI should be selected according to the strategies listed in Table 2 for different ground objects based upon the NDWI time series of each pixel. Finally, this NDWI image is segmented with threshold values to identify offshore drilling rigs. To find the NDWI features that distinguish water, bare land (islands) and offshore drilling rigs, we used 10 m resolution Sentinel-2 MSI images and Google high-resolution images to vectorize the boundary of water, offshore drilling rigs and bare land (islands) samples as the area of interest in the north, central and south Caspian Sea. Then, the areas of interest of the three types of ground objects are superimposed onto the maximum NDWI, minimum NDWI and mean NDWI composite images to calculate the distribution range of their NDWI values. In this sample selection, there are 100,000 water samples, 1050 offshore drilling rig samples and 10,000 bare land (islands) samples. Figure 7 shows the histogram

statistical distribution of the NDWI composite images of the maximum, minimum and mean of various ground objects samples in the waters of the Caspian Sea.

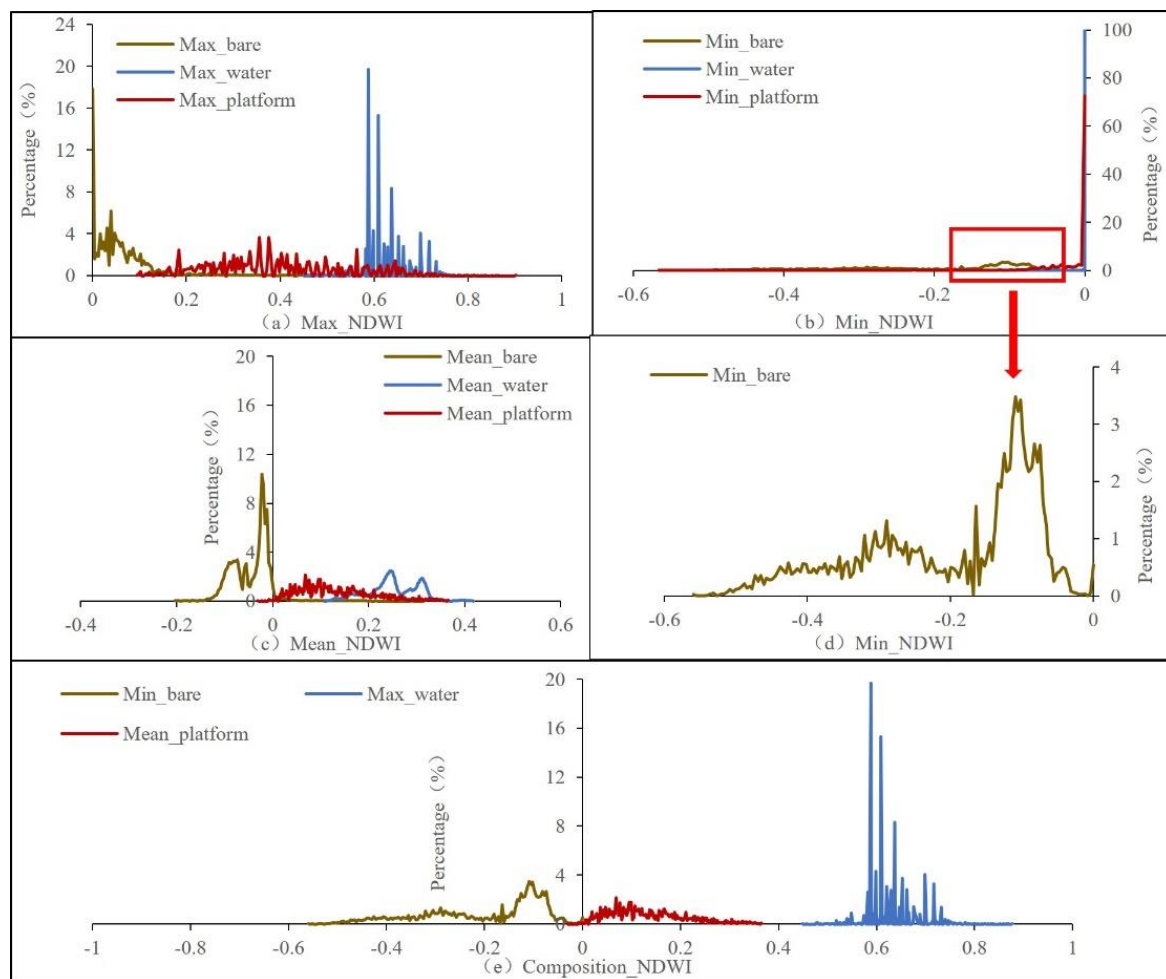


Figure 7. Distributions of maximum, minimum, mean, NDWI values of bare land, water and offshore drilling rig.

From the statistical distribution based on the maximum, minimum and mean NDWI images of water, offshore drilling rigs and bare land (islands) samples (Figure 7a–c), we found that water can be easily separated from bare land and offshore drilling rig in the maximum NDWI statistics, Its maximum NDWI value (Max_NDWI) is usually greater than 0.55, among which the maximum NDWI value of bare land (islands) is less than 0.2, and the NDWI value of most offshore drilling rigs is between the water and bare land (Figure 7a). Therefore, we can draw the line at the maximum NDWI value of 0.55 to separate water from the other two types. The minimum NDWI value of more than 70% pixels of offshore drilling rigs and water is equal to 0 (Figure 7b), while the minimum NDWI value of bare land (island) is usually less than -0.05 (Figure 7d). Therefore, using a minimum NDWI value of -0.05 , we can separate bare land from water and offshore drilling rigs. Similarly, the mean NDWI value of offshore drilling rigs (Mean_NDWI) is between 0–0.4; this can be used to distinguish offshore drilling rigs from bare land (islands) (Figure 7c). It is worth noting that in Figure 7a, the maximum NDWI value of some pixels of offshore drilling rigs is greater than 0.55, mainly due to the mixing of water body pixels in the vectoring process of offshore drilling rig samples. In Figure 7b, the value of water and offshore drilling rig samples in the minimum NDWI statistics is equal to 0, which is possibly due to the quality reduced ETM+ image pixels caused by clouds, shadows, strips, etc. Such pixels must be masked out for further analysis. In Figure 7c, the mean NDWI statistics of water samples

are relatively low (0.2–0.4). The main reason is that the existence of cloud, shadow, strip and other problems leads to partial pixels were masked ($NDWI = 0$), which reduces the value range of the mean NDWI of water. From the statistical results of sample pixels, using any single one of maximum, minimum, or mean NDWI would not make a good distinction between water, bare land (islands) and offshore drilling rigs. However, if we combine different NDWI features (maximum, minimum and mean), we can effectively distinguish water, bare land (islands) and offshore drilling rigs. Therefore, we design a set of rules based on these statistics to depict water bodies ($Max_NDWI > 0.55$), bare land (islands) ($Min_NDWI < -0.05$) and offshore drilling rigs ($0 < Mean_NDWI < 0.4$) to classify the three types (Figure 7e).

3.4. Offshore Drilling Rig Extraction Based on Optimal NDWI Composite

3.4.1. Preliminary Extraction of Offshore Drilling Rigs

In Section 3.3.3, through the statistical analysis of sample pixels, we build a set of rules to effectively distinguish water, bare land (islands) and offshore drilling rigs based on NDWI time series (Maximum, Minimum, Mean). The NDWI time-series features proposed in Section 3.3.3 effectively reduce if not completely remove residual clouds and cloud shadows and other disturbing factors on the NDWI value. Because the optimal NDWI composite image reflects the true NDWI value of the water, bare land (islands) and offshore drilling rigs, the threshold segmentation can then be used to identify the offshore drilling rigs. False alarms such as passing ships and clouds show similar reflectivity characteristics to offshore drilling rigs, which constitutes a major difficulty in identifying of offshore drilling rigs. To better identify offshore drilling rigs, the optimal NDWI composite images were constructed using Landsat-7 ETM+ images for two consecutive years in this paper. The general process is shown in Figure 8. First, the Landsat-7 ETM+ images of the Caspian Sea for two consecutive years were preprocessed to remove most clouds and shadows, and the NDWI was calculated. The map algebra statistics are then performed based on the maximum, minimum and mean NDWI of pixels. Finally, the optimal composite NDWI image is generated according to the following rules: water body ($Max_NDWI > 0.55$), bare land (island) ($Min_NDWI < -0.05$) and offshore drilling rig ($0 < mean_NDWI < 0.4$).

The optimal NDWI compositing strategy is based on this fact: On the one hand, once the offshore drilling rig is built, it will be used for a long time, i.e., generally, about 20 years, and its location and size will remain unchanged. However, passing ships do not stay at a fixed position for a long time, so the optimal NDWI composite method can easily avoid the influence of moving ships. On the other hand, with two consecutive years of Landsat images, we can obtain cloud-free or cloud-less composite images to the greatest extent. The construction of an offshore drilling rig can then be completed within two years at most (acquired through long-term image observation). Therefore, the optimal NDWI composite data established in this paper include all images from one year and the following year. Adopting this strategy, we will avoid ships and reduce the effects of clouds, cloud shadows, etc. Due to a large amount of calculation for the synthesis of optimal composite NDWI images, we implement our algorithm on the GEE cloud platform.

After the optimal NDWI composite is synthesized according to the process shown in Figure 8, the offshore drilling rig can be identified with a threshold segmentation method. Image threshold segmentation is one of the most commonly used image segmentation methods. This study assumes that the optimal composite NDWI image is $F(x, y)$, which is classified into the water, bare land and offshore drilling rigs by setting the corresponding threshold value. The classification image is $g(x, y)$ and the specific formula is as follows:

$$g(x, y) = \begin{cases} \text{Bare land, } NDWI < -0.05 \\ \text{offshore drilling rig, } 0 < NDWI < 0.4 \\ \text{Water, } NDWI > 0.55 \end{cases} \quad (2)$$

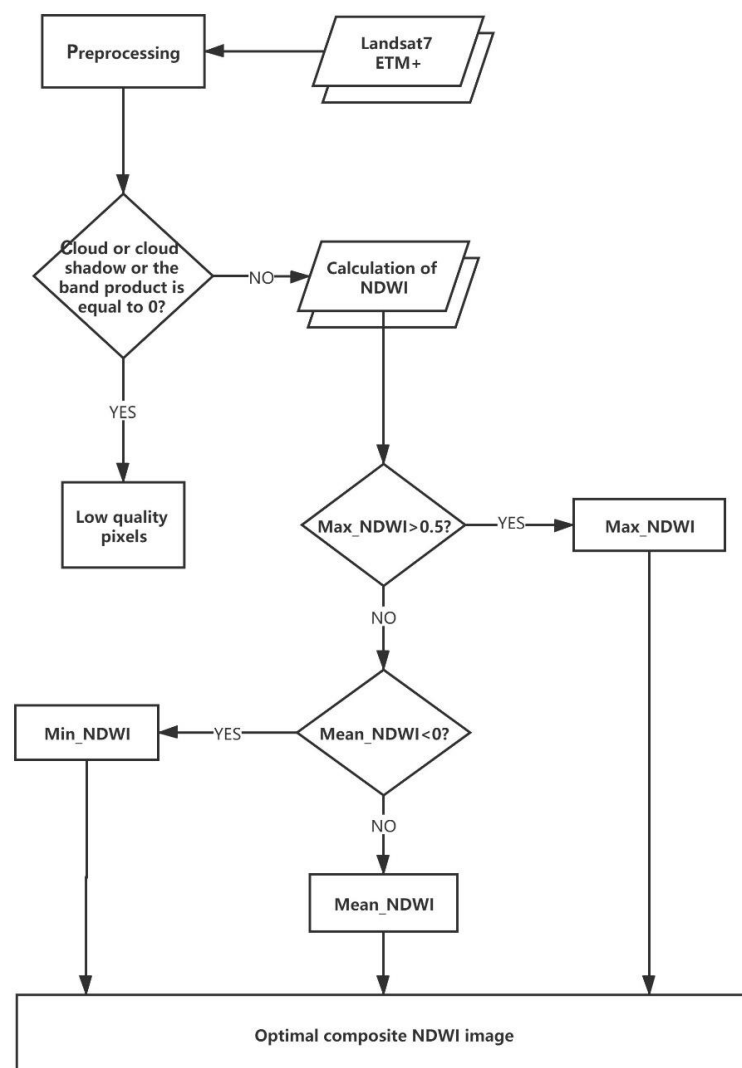


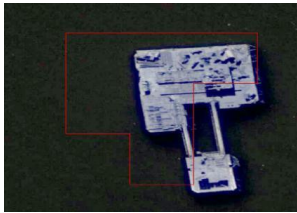
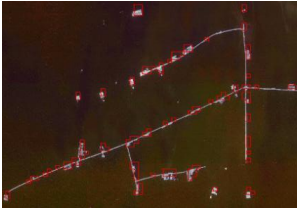
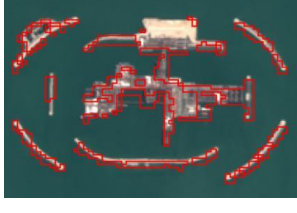
Figure 8. The procedure to generate NDWI composites from multiyear Landsat-7/ETM + imagery.

3.4.2. Postprocessing of Offshore Drilling Rig Detection Results

The Caspian Sea covers a wide area (about 370,000 square kilometers), with more islands and sandbars along the coast, especially in the shallow water area in the northern part. However, the NDWI value of the interface between land edges, islands, or sandbars and water is similar to that of offshore drilling rigs, which tends to be another source of false alarms. Furthermore, there are many offshore drilling rigs in the Caspian Sea and their structures are complex. The offshore drilling rigs with close distances extracted by the threshold segmentation may be different parts of one platform. Therefore, postprocessing of the extracted results is required to improve the detection accuracy, and it mainly includes two parts: (1) Generating a land mask to eliminate the interference of islands, sandbars and near-shore areas from the extraction results; (2) Refining and combining offshore drilling rigs with similar distances. The land mask is generated with a spatial buffer toward the center of the Caspian Sea based on the Caspian Sea vectorized boundary data. While most offshore drilling rigs are located 4 km away from the boundary line of the Caspian Sea (based on visual interpretation with high-resolution images on Google Earth), some of them are relatively closer to the islands and sandbars in the water. If the buffer distance of islands and sandbars is set too large, offshore drilling rigs could be excluded. Therefore, the buffer distance of the Caspian Sea boundary is set as 3.5 km, while the buffer distance of islands and sandbars is set as 60 m.

Based on field photos, high-resolution remote sensing images, EIA, and their shape, structure and combination characteristics, the offshore drilling rigs in the Caspian Sea can be grouped into three categories: single offshore drilling rigs, large offshore drilling rig groups and artificial islands formed by offshore drilling rigs (Table 4). As shown in Table 4, the large offshore drilling rig group is connected by multiple offshore drilling rigs through “corridors”. However, due to the narrow width of the “corridor” (about 9 m), only the platforms can be successfully identified. The artificial island is equipped with corresponding auxiliary facilities and the basic equipment for oil production (gas), and the identification results are often broken. Therefore, we establish the following rules for large offshore drilling rig groups and artificial island formed by offshore drilling rigs detected in remote sensing images, to better determine the type and number of offshore drilling rigs: (1) For large offshore drilling rigs, vectorized “corridors” will be built. A 60 m buffer zone will be built on both sides with the vectorized corridor as the center. Offshore drilling rigs in the buffer zone will be grouped into the large offshore drilling rig group, while offshore drilling rigs outside the buffer zone will be counted as single offshore drilling rigs. (2) For the artificial island of offshore drilling rig, each polygon of the artificial island is identified to build a 150 m buffer zone and then fused and counted as one offshore drilling rig.

Table 4. Caspian offshore drilling rig types and image characteristics (the red border in remote sensing images is the preliminary extraction result).

Platform Type	Remote Sensing Image	Related Images
Single offshore drilling rig		
Large offshore drilling rig group		
Artificial island of offshore drilling rig		

4. Results and Discussion

4.1. Identification Accuracy Analysis

To explore the effect of the optimal NDWI algorithm on offshore drilling rig identification, we evaluate the accuracy of offshore drilling rig identification in the Caspian Sea waters in 2018. Because there is no ground truth data and field verification is difficult to carry out, we adopt the following verification strategy. It includes partial verification in near-shore areas with Google Earth images, visual interpretation of Sentinel-2 MSI and self-consistency verification of Sentinel-2 MSI (mainly for relatively remote and small platforms offshore). For this purpose, a total of 7405 potential targets are extracted based on the Landsat-7 ETM+ optimal NDWI composite. From these, 6883 targets of the extracted

targets are excluded using the buffer mask of land, islands and sandbanks. Finally, 522 potential offshore drilling rigs are confirmed by refining the processing rules of offshore drilling rigs. After verification with high-resolution images, the final algorithm determines 497 offshore drilling rigs, including 486 single platforms, 3 large offshore drilling rig groups and 8 artificial island platforms (Figure 9).

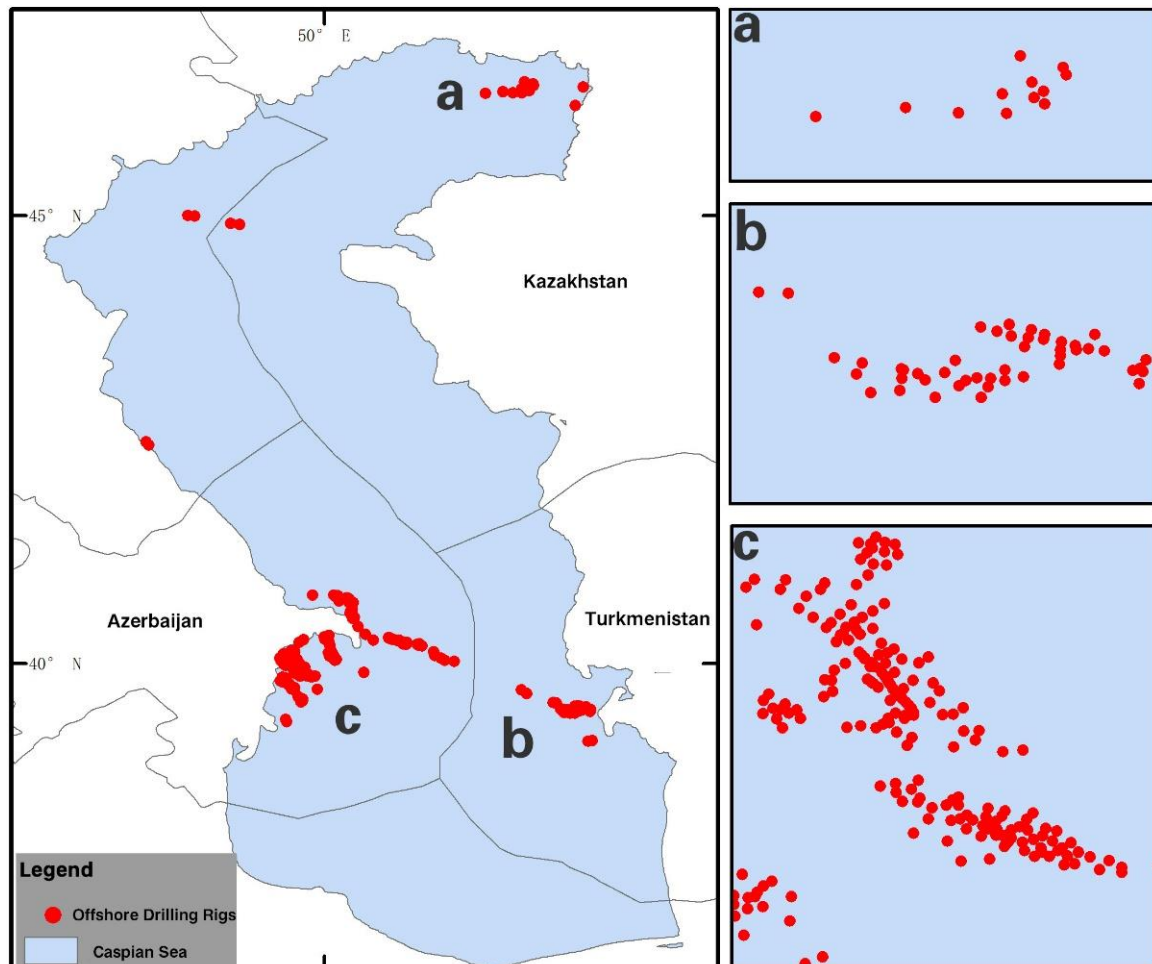
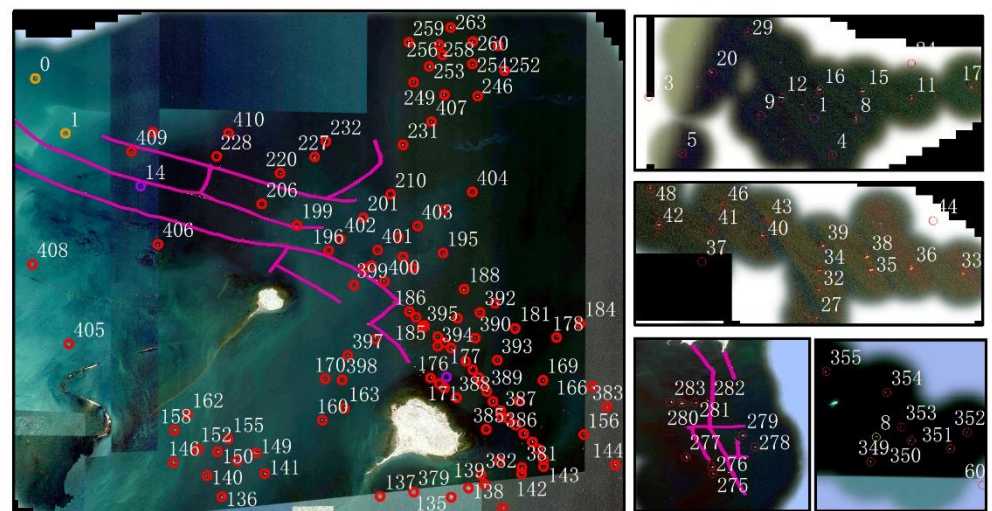


Figure 9. Offshore drilling rig extraction results, figures (a), (b), and (c) are respectively enlarged areas (a), (b), and (c) in the left image.

We further check the extracted offshore drilling rigs through Google Earth's high-resolution images (Figure 10). Careful visual inspection reveals that the 3.5 km buffer distance of the Caspian Sea and the 60 m buffer distance of the islands preclude a large number of false alarms, such as those of docks, berthing vessels, islands or sandbars at the water junction (brown dots in the image). But at the same time, some offshore drilling rigs (13) off the coast of Azerbaijan have been excluded, because they are too close to shorelines. Based on Google Earth images, in the water area beyond the buffer distance, there are 248 offshore drilling rigs (including two offshore drilling rig groups), 238 of which were extracted correctly, while 10 were undetected and 23 were misidentified. The 23 misidentified targets are all small and narrow pieces of land in the water (generally no more than 2 pixels in width, i.e., 60 m).

Verification of Google Earth Images(2017,2018)



The enlarge Google Earth images of some offshore drilling rigs



Figure 10. Google Earth image verification results.

Sentinel-2 MSI images are mainly used for visual interpretation and self-consistency verification (Figure 11). All offshore drilling rigs not confirmed by Google Earth images are loaded onto the high-quality Sentinel-2 true-color images (spatial resolution 10 m). Through careful visual verification, a total of 265 offshore drilling rigs were found, among which 259 offshore drilling rigs (including one offshore drilling rig group) were correctly extracted by the proposed algorithm, while six offshore drilling rigs were omitted and two were misidentified.

To summarize, there are 526 offshore drilling rigs in the Caspian Sea covered by the Landsat images, among which 497 offshore drilling rigs were automatically identified by the proposed algorithm, while 29 offshore drilling rigs were omitted (including 13 offshore drilling rigs being masked out) and 25 were misidentified (Table 5). The accuracy rate was 90.2%, the false-negative rate (including the buffer mask platforms) was 5.3%, and the misidentification rate was 4.5%.

4.2. Comparison with Other Methods

4.2.1. Comparison with the Method Based on SAR Images

Wong et al. [17] extracted the offshore drilling rigs using Sentinel-1 SAR data with GEE. The method may be divided into five steps: (1) Generating median composite image; (2) Calculating the difference between median composite image and mean filter image; (3) The difference image is segmented by static or dynamic threshold; (4) Eroding and dilating the segmentation result; and (5) The center of the connected area is extracted as the location of the drilling platform. We applied their method to the test area. The test area, as shown in Figure 12a, contains a large offshore drilling rig group and a number of scattered individual offshore drilling rigs. Therefore, it is suitable for testing the performance of the algorithm.

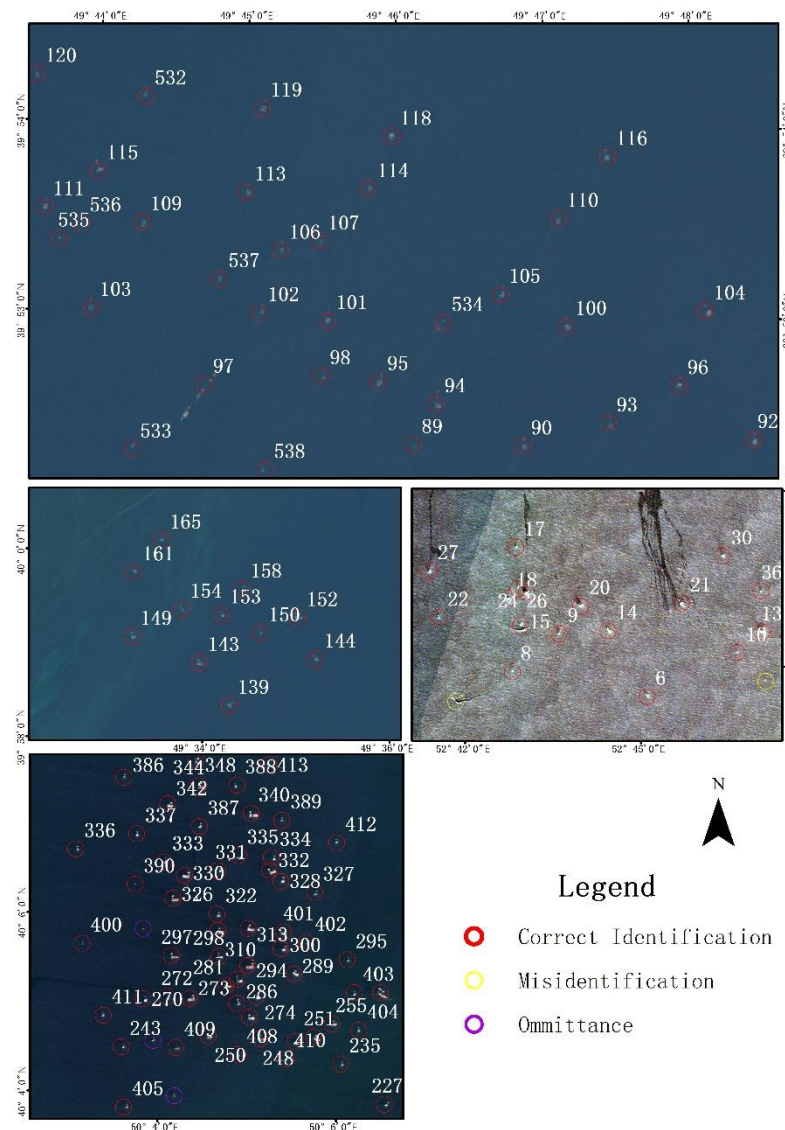


Figure 11. Sentinel-2 verification results.

Table 5. Identification results of offshore drilling rigs.

Verification Image	Visual Interpretation	Successfully Identified	Missed	False Identification	Accuracy (%)
Google Earth	248	238	23	23	
Sentinel-2	265	259	6	2	90.2%
Total	513	497	29	25	

The results are shown in Figure 12b. We can see that due to the erosion and dilation operation for the preliminary extraction results, the interconnected platforms are interrupted and identified as a single drilling rig. We adopt different strategies to postprocess the preliminary extraction results and set buffers to merge adjacent platforms, so that the number of platforms is more accurate. Sensitivity to parameters is the biggest disadvantage of Wong’s method. The size of filtering window and the shape and size of morphological operation structure elements will affect the results. In [17], 460 parameter combinations were tested and the optimal parameter combination was selected. However, the portability of the optimal parameter combination in other regions is uncertain.

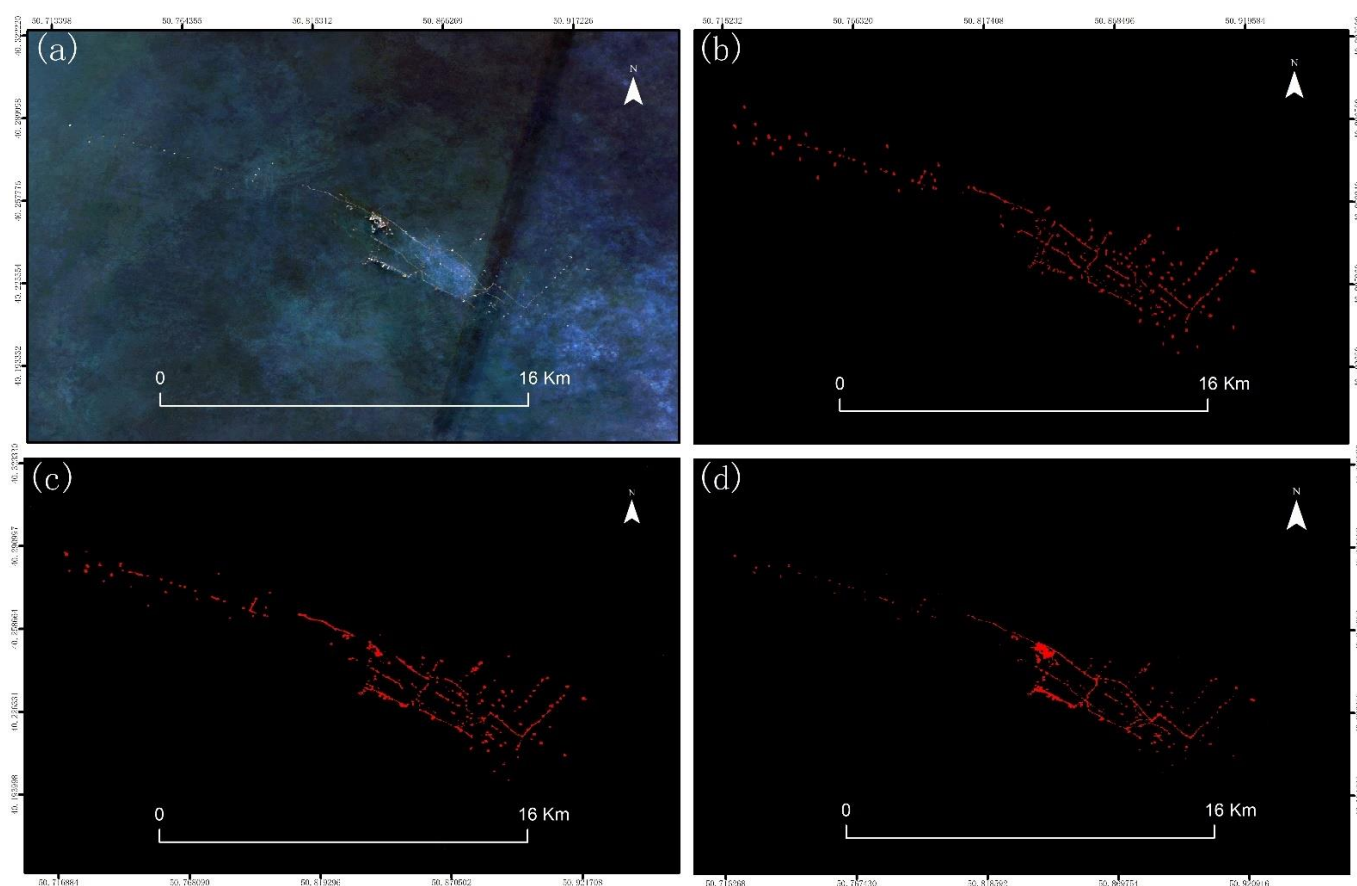


Figure 12. The results of our method compared with the other two methods. (a) is a color composite image of the Sentinel-2 MSI image of the test area. (b) is the identification result of TSRS method. (c) is the identification result based on Sentinel-1 SAR image. (d) is the identification result of our method.

4.2.2. Comparison with the Method Based on Optical Remote Sensing Data

Liu et al. [21] extracted offshore drilling rigs using Landsat time-series and multirefinement strategies. Specifically, they extracted the sea surface targets according to the relatively high reflectance compared to the surrounding water. They then adopted an image time-series strategy to eliminate moving vessel to get potential candidate targets with a simple overlay analysis by using pairwise comparison, according to the position-invariant principle of offshore drilling rigs. Finally, a compound refinement, in which all the pairwise comparison binary images were accumulated to calculate the occurrence frequency and set the double threshold to extend the position- and size-invariant principle to a temporal dimension, was used to maximize the exclusion of random residual clouds. In this method, the final determination of offshore drilling rigs requires a pairwise comparison between images, and each comparison requires mathematical morphology operation. Then the double threshold and area variation amplitude need to be manually set. These steps increase the computation and subjectivity of the method, such as the setting of the structural elements of mathematical morphology operation, double thresholds and the fluctuation range of offshore drilling rig area. As a comparison, our proposed algorithm is simple in operation, and the discriminant rules of offshore drilling rig are based on the statistical analysis of samples, which is less subjective.

Liu et al. [37] proposed the method to assess the platform state based on the time-series remote sensing (TSRS). This method includes three steps: the first two are to identify the location of the offshore drilling rigs, and the last is to determine their current state. In contrast to our detection method, it does not involve the assessment of the status of the rig, and does not take into account the different data sources used. We opted to use the first

two steps of the TSRS method to detect the offshore drilling rigs in the experimental area in order to perform a comparison with our method.

The first step of the TSRS method is to detect the candidate targets of the offshore drilling rigs from individual images. In order to achieve this purpose, the TRSR method uses the Order Statistic Filtering (OSF) method to estimate the sea background, and adaptively sets the threshold according to the OSF value of the sliding window and the constant value of noise. It is worth noting that the percentage value of OSF and noise values are set subjectively. The second step of the TSRS method is to segment the offshore drilling rigs from the time series images. In this step, the binary images of the detection results of all individual images are accumulated. The fixed threshold segmentation for the accumulated image will be applied to obtain the final detection results. Because TSRS method uses more than 20 years of multisource data, in addition to detecting the drilling platform, it also monitors the existence status of the drilling platform. Our purpose is to propose a drilling platform detection algorithm based on two consecutive years of Landsat images without paying attention to its dynamic changes. Therefore, we only use two consecutive years of Landsat data in the modified area when testing TSRS method. Figure 12c presents the results obtained using the TSRS method. Compared with our method (Figure 12d), it can be seen that in the middle part of the test area, the TSRS method does not extract the whole platform, and the extraction effect of the connecting channel of the drilling platform group is not as good as in our method. The biggest disadvantage of the TSRS method is its sensitivity to various parameter settings; there are many artificial parameters. In [37], the author conducted experiments on parameter setting and selected the optimal parameters. However, once the study area changes, the suitability of this parameter combination cannot be determined. The result of TRSR method obtained in the test area may also be obtained through experiments with different parameters. The optimal NDWI synthesis required by our method comes from the statistical analysis of samples, and does require a subjective selection of parameters.

Elvidge [34] detected global combustion flames of associated waste gas (VIIRS ignition point data) during the oil and gas extraction and treatment processes with the VIIRS VNF algorithm and generated a set of global VIIRS ignition point data set. The VIIRS ignition point data in 2018 showed only a total of 19 associated waste gas ignition points in the Caspian waters. Sentinel-2 image verification found that 17 of the 19 associated waste gas ignition points were offshore drilling rigs with associated waste gas combustion, while two associated waste gas ignition points were misidentified (Figure 13a,b). In terms of the number of offshore drilling rigs in Caspian waters, the 17 offshore drilling rigs identified by the VIIRS VNF algorithm were also successfully identified by our proposed algorithm (Figure 13). Moreover, our algorithm can identify offshore drilling rigs more effectively (497 vs. 17) and is not limited to those with associated waste gas combustion flames. The position accuracy of offshore drilling rigs extracted by our proposed algorithm is also higher than that of the VIIRS ignition point data. When the distance of multiple offshore drilling rigs is relatively close, the positional accuracy of the VNF algorithm is much poorer. Furthermore, by comparing VIIRS ignition point data of different years in Caspian Waters from 2012 to 2016, 2017 and 2018, it is also found that the location accuracy needs to be further optimized (Figure 13r,s).

4.3. Missed and False Identification of Offshore Drilling Rigs

A total of 29 offshore drilling rigs are found to be missing by Google Earth and Sentinel-2 image verification, among which 13 were masked out by the buffer zones near the Caspian Sea coasts, while the other 14 were mainly due to their small-size, i.e., length or width generally less than a single 30 m by 30 m image pixel (Figure 14a). The remaining two offshore drilling rigs cannot be examined due to the low spatial resolution of Sentinel-2 images. This shows that the wrongly identified offshore drilling rigs are mainly either small narrow islands or small exposed islands with shallow near shore water in the shape of a circle. For the narrow small islands, the width is generally nearly or less than a pixel

size (30 m), and the length is generally larger than a pixel size. They are mainly distributed in the west of the Caspian Sea near the coast (Figure 14b). To solve these problems, remote sensing imagery with a much finer spatial resolution is required.

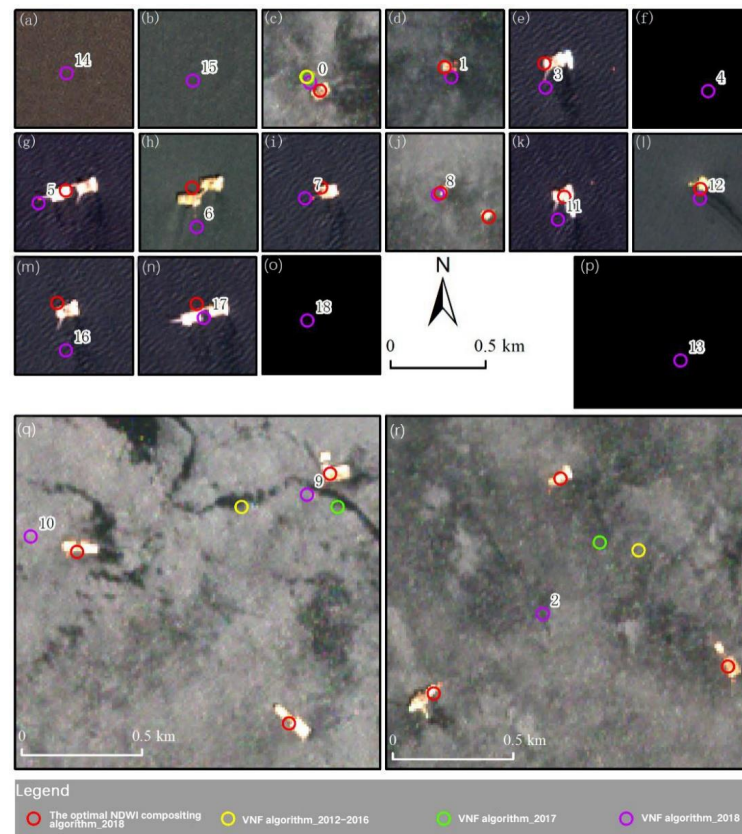


Figure 13. A comparison of results from different algorithms on extracting offshore rigs in the Caspian Sea. (a–r) are the comparison between the recognition results of VNF algorithm and those of our algorithm, it can be seen that VNF algorithm has a large number of error recognition.



Figure 14. Validation of undetected platforms and misidentified platforms. (a) are the omitted offshore drilling rigs of our method, (b) are the misidentified offshore drilling rigs of our method.

5. Conclusions

The world is in an era of global climate change; at the same time, we are witnessing a rapidly growing process of globalization. However, in recent years, the globalization process has arrived at a crossroads, with increasing uncertainties in many areas. The global oil market is one of those areas; it has dramatically affected the world crude oil market, which has been on something of a roller coaster ride in recent years. There is a pressing need to understand with accuracy global fossil fuel production worldwide. Remote sensing data have been an effective resource for monitoring oil and gas extraction activities. But existing methods for the detection of offshore drilling rigs from optical remote sensing images are still limited, in terms of either their automation or spatial details. The availability of cloud computing facilities calls for high-efficiency algorithms to extract information from fine resolution optical remote sensing images obtained by an increasing number of satellite sensors.

This study proposed a new automatic method to synthesize nominal annual optimal NDWI images from multitemporal Landsat-7 ETM+ data to distinguish offshore drilling rigs from the water background. The advantages of this algorithm are as follows:

1. A NDWI characteristics statistical analysis was carried out on the main disturbance ground object (water and bare ground) in order to identify offshore drilling rigs against the background of ocean or water, and a set of rules was established to effectively distinguish three objects to depict water ($\text{Max_NDWI} > 0.55$), bare ground ($\text{Min_NDWI} < -0.05$) and offshore drilling rig ($0 < \text{Mean_NDWI} < 0.4$). These rules can not only effectively distinguish water, bare land (islands) and offshore drilling rigs, but can also effectively select clean pixels from images partially polluted by clouds and cloud shadows to generate high quality NDWI composites. These high quality NDWI composites form the basis of a method to identify offshore drilling rigs with an overall accuracy reaching 90.2%.
2. The optimal NDWI compositing process considers images that were taken over two consecutive years, successfully excluding passing ships, clouds and cloud shadows, and other moving objects.
3. The algorithm uses free ETM+ images to facilitate the monitoring of long time series. The optimal NDWI compositing rules are set based on a statistical analysis of the sample pixels in the region of interest, avoiding human subjectivity. Meanwhile, the algorithm is simple and easy to implement, and the GEE platform provides powerful computation. Furthermore, a spatial resolution of 30 m can effectively avoid missed identification with a coarse spatial resolution of night-light data. It also overcomes the defect that night-light ignition point data cannot identify offshore drilling rigs without a waste gas flame.
4. One current limitation is the robustness of the method, which needs to be further confirmed. The algorithm was only used in the Caspian Sea with good water quality; future work should focus on the large-scale research of other sea areas such as the Gulf of Mexico or the Persian Gulf. Another limitation is that Landsat-7 ETM+ images are only used for static identification of oil and gas platforms in the Caspian region. The next step is to use multisource remote sensing images, such as Sentinel-2 imagery, Landsat-8 OLI imagery and SAR imagery, to conduct more comprehensive research of offshore oil and gas platforms so as to improve the recognition accuracy and time length in order to obtain temporal and spatial dynamic attribute information and establish a more complete global oil and gas platform information management system. Lastly, it is rather difficult to determine a distance for near-shore areas. An unsuitable buffer distance can miss rigs or make false identifications. As such, the method yielded results that were highly accurate in open waters but relatively inaccurate near the shore.

The composite NDWI synthesis method proposed in this paper can be used to identify and dynamically monitor offshore drilling rigs within a large water surface area relatively quickly, which is of great significance for exploring the exploitation status of offshore oil

and gas resources. It can be extended to finer spatial resolution optical remote sensing images; thus, small-sized drilling rigs can also be effectively detected. Of course, there are still some issues with this algorithm. For example, the threshold segmentation of the optimal composite NDWI image for offshore drilling rig identification will simultaneously identify some islands, sandbars, parts of the boundary between coastal areas and water, and scattered exposed islands around them. Furthermore, an offshore drilling rig may be identified as multiple discrete rigs, which requires postprocessing of preliminary results, increasing the workload. We only tested this algorithm in the Caspian Sea, and it needs further validation whether in order to be applied in other regions.

Author Contributions: Conceptualization, H.Z., G.J. and Q.Z.; methodology, H.Z. and Q.Z.; software, H.Z. and G.J.; validation, H.Z., G.J. and S.Z.; formal analysis, H.Z., G.J. and X.L.; data curation, H.Z.; writing—original draft preparation, G.J.; writing—review and editing, G.J. and Q.Z.; visualization, H.Z. and G.J.; supervision, Q.Z.; project administration, Q.Z. and Y.S.; funding acquisition, Q.Z. and Y.S. All authors have read and agreed to the published version of the manuscript.

Funding: This work was supported by the National Key Research and Development Program of China (Grant No. 2017YFB0504204); the One Hundred Talents Program of the Chinese Academy of Sciences (2015, Grant No. Y674141001); and supported in part by the National Natural Science Foundation of China (General Program, Grant No. 42071351), the National Key Research and Development Program of China (Grant No. 2020YFA0608501), the Liaoning Revitalization Talents Program (Grant No. XLYC1802027) and the One Hundred Talents Program of Chinese Academy of Sciences (Grant No. Y938091).

Institutional Review Board Statement: Not applicable.

Informed Consent Statement: Not applicable.

Acknowledgments: The authors would like to thank the Google Earth Engine for providing the computing platform and integrating free satellite imagery data and the editors and reviewers for their comments and suggestions.

Conflicts of Interest: The authors declare no conflict of interest.

References

- Jiang, W.; Zhou, W.; Jia, H. Potential of Global Offshore Petroleum Resource Exploration and Utilization Prospect. *Nat. Gas. Geosci.* **2010**, *21*, 988–995.
- Sun, C.; Liu, Y.; Zhao, S.S.; Song, J. Estimating offshore oil production using DMSP-OLS annual composites. *ISPRS J. Photogramm.* **2020**, *165*, 152–171. [[CrossRef](#)]
- BP. Energy Outlook 2019 Edition. 2019. Available online: <https://www.bp.com/content/dam/bp/business-sites/en/global/corporate/pdfs/energy-economics/energy-outlook/bp-energy-outlook-2019.pdf> (accessed on 13 December 2020).
- EIA. International Energy Outlook 2018. 2018. Available online: https://www.eia.gov/pressroom/presentations/capuano_0724_2018.pdf (accessed on 19 November 2019).
- World Bank Database. Available online: <https://databank.worldbank.org/home.aspx> (accessed on 13 December 2020).
- Gorelick, N.; Hancher, M.; Dixon, M.; Ilyushchenko, S.; Thau, D.; Moore, R. Google Earth Engine: Planetary-scale geospatial analysis for everyone. *Remote Sens. Environ.* **2017**, *202*, 18–27. [[CrossRef](#)]
- Liu, Y.; Cui, H.Y.; Kuang, Z.; Li, G.Q. Ship detection and classification on optical remote sensing images using deep learning. *ITM Web Conf. EDP Sci.* **2017**, *12*, 05012. [[CrossRef](#)]
- Gallejo, A.J.; Pertusa, A.; Gil, P. Automatic Ship Classification from Optical Aerial Images with Convolutional Neural Networks. *Remote Sens.* **2018**, *10*, 511. [[CrossRef](#)]
- Gao, L.; He, Y.; Sun, X.; Jia, X. Incorporating Negative Sample Training for Ship Detection Based on Deep Learning. *Sensors* **2019**, *19*, 684. [[CrossRef](#)] [[PubMed](#)]
- Huang, G.A.; Wan, Z.A.; Liu, X.A.; Hui, J.B. Ship detection based on squeeze excitation skip-connection path networks for optical remote sensing images. *Neurocomputing* **2019**, *332*, 215–223. [[CrossRef](#)]
- Falqueto, L.E.; Sá, J.A.; Paes, R.L.; Passaro, A. Oil rig recognition using convolutional neural network on Sentinel-1 SAR images. *IEEE Geosci. Remote Sens. Lett.* **2019**, *16*, 1329–1333. [[CrossRef](#)]
- Peng, C.; Wang, J.; Li, D. Oil platform investigation by multi-temporal SAR remote sensing image. In Proceedings of the Conference on SAR Image Analysis, Modeling, and Techniques XI, Prague, Czech Republic, 21–22 September 2011.
- Wang, J.; Liu, Y.; Li, M.; Yang, K.; Cheng, L. Drilling platform detection based on ENVISAT ASAR remote sensing data: A case of southeastern Vietnam offshore area. *Geogr. Res.* **2013**, *32*, 2143–2152.

14. Wang, Q.; Zhang, J.; Su, F. Offshore Platform Extraction Using RadarSat-2 SAR Imagery: A Two-Parameter CFAR Method Based on Maximum Entropy. *Entropy* **2019**, *21*, 556. [CrossRef]
15. Cheng, L.; Yang, K.; Tong, L.; Liu, Y.; Li, M. Invariant triangle-based stationary oil platform detection from multitemporal synthetic aperture radar data. *J. Appl. Remote Sens.* **2013**, *7*, 073537. [CrossRef]
16. Wan, J.; Yao, P.; Meng, J. Research on Detection Method of the Offshore Oil Platform Based on SAR Images. *Bull. Surv. Map.* **2014**, *1*, 56–59.
17. Wong, B.A.; Thomas, C.; Halpin, P. Automating offshore infrastructure extractions using synthetic aperture radar & Google Earth Engine. *Remote Sens. Environ.* **2019**, *233*, 111–412.
18. Zhang, J.; Wang, Q.; Su, F. Automatic extraction of offshore platforms in single SAR images based on a dual-step-modified model. *Sensors* **2019**, *19*, 231. [CrossRef] [PubMed]
19. Meng, R.; Xing, Q. Detection of offshore ship and well platform based on optical remote sensing images. *J. Comput. Appl.* **2013**, *33*, 708–711. [CrossRef]
20. Cheng, W. Research on Extraction of Oil and Gas Drilling Platforms with Remote Sensing in the South China Sea. Master's Thesis, Nanjing University, Nanjing, China, 2015.
21. Liu, Y.X.; Sun, C.; Yang, Y.; Zhou, M.; Zhan, W.; Cheng, W. Automatic extraction of offshore platforms using time-series Landsat-8 Operational Land Imager data. *Remote Sens. Environ.* **2016**, *175*, 73–91. [CrossRef]
22. Zhao, S.; Sun, C.; Wang, H.; Cheng, W. Extraction and Monitoring of Offshore Oil and Gas Platforms Based on Landsat Imagery. *Trop. Geogr.* **2017**, *37*, 112–119.
23. Li, Q. Oil and Gas Platforms Detection and Oil and Gas Resources Security Situation Evaluate Based on Multi-Source Data in the South China Sea. Master's Thesis, Lanzhou Jiaotong University, Lanzhou, China, 2016.
24. Sun, C. Dynamic Monitoring of Oil/Gas Development in the South China Sea Based on Long-Period Time-Serious and Multi-Source Remote Sensing Image. Ph.D. Thesis, Nanjing University, Nanjing, China, 2018.
25. Fan, Y.; Wang, Q. A Connected Component Based Offshore Platforms Extraction Method of GF2 Multi-channel Optical Images. In Proceedings of the 2019 IEEE 4th International Conference on Signal and Image Processing (ICSIP), Wuxi, China, 19–21 July 2019; IEEE: New York, NY, USA, 2019; pp. 916–919.
26. Zhu, Z.; Tang, Y.; Han, T. Offshore Platform Detection Based on Harris Detector and Intensity-Texture Image from Sentinel_2A Image. In Proceedings of the 2018 10th IAPR Workshop on Pattern Recognition in Remote Sensing (PRRS), Beijing, China, 19–20 August 2018; IEEE: New York, NY, USA, 2018; pp. 1–4.
27. Croft, T.A. Nighttime images of the earth from space. *Sci. Am.* **1978**, *239*, 86–101. [CrossRef]
28. Stroppiana, D.; Pinnock, S.; Gregoire, J.M. The Global Fire Product: Daily fire occurrence from April 1992 to December 1993 derived from NOAA AVHRR data. *Int. J. Remote Sens.* **2010**, *21*, 1279–1288. [CrossRef]
29. Chowdhury, S.; Shipman, T.; Chao, D.; Elvidge, C.D.; Zhizhin, M.; Hsu, F.C. Daytime Gas Flare Detection Using Landsat-8 Multispectral Data. In Proceedings of the IEEE Joint International Geoscience and Remote Sensing Symposium (IGARSS), Quebec City, QC, Canada, 13–18 July 2014.
30. Casadio, S.; Arino, O.; Minchella, A. Use of ATSR and SAR measurements for the monitoring and characterisation of night-time gas flaring from offshore platforms: The North Sea test case. *Remote Sens. Environ.* **2012**, *123*, 175–186. [CrossRef]
31. Anejionu, O.C.D.; Blackburn, G.A.; Whyatt, J.D. Detecting gas flares and estimating flaring volumes at individual flow stations using MODIS data. *Remote Sens. Environ.* **2015**, *158*, 81–94. [CrossRef]
32. Elvidge, C.D.; Ziskin, D.; Baugh, K.E.; Tuttle, B.T.; Ghosh, T.; Pack, D.W.; Erwin, E.H.; Zhizhin, M. A Fifteen Year Record of Global Natural Gas Flaring Derived from Satellite Data. *Energies* **2009**, *2*, 595–622. [CrossRef]
33. Elvidge, C.D.; Zhizhin, M.; Hsu, F.C.; Baugh, K.E. VIIRS Nightfire: Satellite Pyrometry at Night. *Remote Sens.* **2013**, *5*, 4423–4449. [CrossRef]
34. Elvidge, C.D.; Zhizhin, M.; Baugh, K.; Hsu, F.C.; Ghosh, T. Methods for Global Survey of Natural Gas Flaring from Visible Infrared Imaging Radiometer Suite Data. *Energies* **2016**, *9*, 14. [CrossRef]
35. Hu, R.; Jiang, F.; Wang, Y.; Li, J.; Li, Y.; Abdimijit, A.; Luo, G.; Zhang, J. Arid Ecological and Geographical Conditions in Five Countries of Central Asia. *Arid Zone Res.* **2014**, *31*, 1–12.
36. EIA. Caspian Sea Region. Available online: https://www.eia.gov/international/content/analysis/regions_of_interest/Caspian_Sea/caspian_sea.pdf (accessed on 23 August 2013).
37. Liu, Y.X.; Hu, C.M.; Sun, C.; Zhan, W.F.; Sun, S.J.; Xu, B.H.; Dong, Y.Z. Assessment of offshore oil/gas platform status in the northern Gulf of Mexico using multi-source satellite time-series images. *Remote Sens. Environ.* **2018**, *208*, 63–81. [CrossRef]
38. Lee, D.S.; Storey, J.C.; Choate, M.J.; Hayes, R.W. Four years of Landsat-7 on-orbit geometric calibration and performance. *IEEE Trans. Geosci. Remote Sens.* **2004**, *42*, 2786–2795. [CrossRef]
39. Morel, A.C.; Fisher, J.B.; Malhi, Y. Evaluating the potential to monitor aboveground biomass in forest and oil palm in Sabah, Malaysia, for 2000–2008 with Landsat ETM+ and ALOS-PALSAR. *Int. J. Remote Sens.* **2012**, *33*, 3614–3639. [CrossRef]
40. Nooni, I.K.; Duker, A.A.; Van Duren, I.; Addae-Wireko, L.; Osei Jnr, E.M. Support vector machine to map oil palm in a heterogeneous environment. *Int. J. Remote Sens.* **2014**, *35*, 4778–4794. [CrossRef]
41. Zhang, Q.L.; Li, B.; Thau, D.; Moore, R. Building a Better Urban Picture: Combining Day and Night Remote Sensing Imagery. *Remote Sens.* **2015**, *7*, 11887–11913. [CrossRef]

42. GEE. Landsat Collections. Available online: <https://developers.google.com/earth-engine/datasets/catalog/landsat-7> (accessed on 27 December 2019).
43. National Oceanic and Atmospheric Administration (NOAA). Available online: https://www.ngdc.noaa.gov/eog/viirs/download_dnb_composites.html (accessed on 2 February 2020).
44. GEE. Sentinel Collections. Available online: <https://developers.google.com/earth-engine/datasets/catalog/sentinel-2> (accessed on 23 November 2019).
45. Markham, B.L.; Storey, J.C.; Williams, D.L.; Irons, J.R. Landsat sensor performance: History and current status. *IEEE Trans. Geosci. Remote Sens.* **2004**, *42*, 2691–2694. [[CrossRef](#)]
46. Zhu, Z.; Wang, S.X.; Woodcock, C.E. Improvement and expansion of the Fmask algorithm: Cloud, cloud shadow, and snow detection for Landsats 4-7, 8, and Sentinel 2 images. *Remote Sens. Environ.* **2015**, *159*, 269–277. [[CrossRef](#)]
47. Zhu, Z.; Woodcock, C.E. Object-based cloud and cloud shadow detection in Landsat imagery. *Remote Sens. Environ.* **2012**, *118*, 83–94. [[CrossRef](#)]
48. Lu, S.L.; Wu, B.F.; Yan, N.N.; Wang, H. Water body mapping method with HJ-1 A/B satellite imagery. *Int. J. Appl. Earth Obs.* **2011**, *13*, 428–434. [[CrossRef](#)]
49. Xu, H.Q. A Study on Information Extraction of Water Body with the Modified Normalized Difference Water Index (MNDWI). *J. Remote Sens.* **2005**, *9*, 589–595.
50. Gao, B.C. NDWI—A normalized difference water index for remote sensing of vegetation liquid water from space. *Remote Sens. Environ.* **1996**, *58*, 257–266. [[CrossRef](#)]
51. Ju, J.; Roy, D.P. The availability of cloud-free Landsat ETM plus data over the conterminous United States and globally. *Remote Sens. Environ.* **2008**, *112*, 1196–1211. [[CrossRef](#)]
52. Wei, J.; Huang, W.; Li, Z.; Sun, L.; Zhu, X.; Yuan, Q.; Liu, L.; Cribb, M. Cloud detection for Landsat imagery by combining the random forest and superpixels extracted via energy-driven sampling segmentation approaches. *Remote Sens. Environ.* **2020**, *248*, 112005. [[CrossRef](#)]
53. Candra, D.S.; Phinn, S.; Scarth, P. Cloud and cloud shadow masking for Sentinel-2 using multitemporal images in global area. *Int. J. Remote Sens.* **2020**, *41*, 2877–2904. [[CrossRef](#)]
54. Holben, B.N. Characteristics of Maximum-Value Composite Images from Temporal Avhrr Data. *Int. J. Remote Sens.* **1986**, *7*, 1417–1434. [[CrossRef](#)]